Thrust Generation due to Airfoil Flapping

Ismail H. Tuncer* and Max F. Platzer[†]

U.S. Naval Postgraduate School, Monterey, California, 93943-5106

Thrust generation on a single flapping airfoil and a flapping/stationary airfoil combination in tandem is studied parametrically. A multiblock Navier–Stokes solver is employed to compute unsteady flowfields. The unsteady flowfield around a single flapping airfoil is also computed by an unsteady potential flow code. The numerical solutions predict thrust generation in flapping airfoils and a significant augmentation of thrust in flapping/stationary airfoil combinations in tandem. The propulsive efficiency is found to be a strong function of reduced frequency and the amplitude of the flapping motion. At a flapping amplitude of 0.40 chord lengths and a reduced frequency of 0.10, the propulsive efficiency of a single NACA 0012 airfoil was computed to be more than 70%. For the airfoil combination in tandem, the propulsive efficiency was augmented more than 40% at a reduced frequency of 0.75 and a flapping amplitude of 0.20 chord lengths when the airfoils are separated by about two chord lengths.

Introduction

THE thrust generation due to airfoil flapping was first recognized by Knoller[1] and Betz[2] in explaining a bird's ability to generate a propulsive force by means of wing flapping. However, the first theoretical investigations of the aerodynamics of flapping wings based on flat-plate airfoil theory by von Kármán and Burgers[3] and Garrick[4] showed that the propulsive efficiency of a flapping airfoil is rather poor (not exceeding 50%) unless the wings are flapped very slowly. During World War II Schmidt[5] proposed the tandem airfoil arrangement, and he demonstrated experimentally that a stationary airfoil positioned in the wake of a flapping airfoil doubles the propulsive efficiency of the single flapping airfoil because the stationary airfoil converts the vortical energy generated by the flapping airfoil into additional thrust. This experimental finding was confirmed by the theoretical analysis of Bosch,[6] who showed by means of an oscillatory flat-plate analysis that a sinusoidally flapping airfoil upstream of a stationary airfoil increases the propulsive efficiency of such an arrangement to almost 100%.

Additional interest in a better understanding of the propulsive and lift interference effects caused by helicopter blades subjected to higher harmonic control was generated by Wood et al.,[7] who found in flight tests of an OH-6A helicopter significant reductions in main rotor shaft torque and engine power. In a recent paper, Wood et al.[8] showed that these power reductions can be explained by the propulsive effects generated by blade flapping and by favorable wake interference effects.

The aerodynamic interference effects between two airfoils are also of great practical interest in many aeronautical applications. Prominent examples are the interference effects between the leading- or trailing-edge devices and the main airfoil on high-lift systems, the interference effects on canard-wing and wing-tail configurations, the blade-vortex interactions on helicopter blades, and the blade row interactions that occur in axial jet engines.

There is, therefore, a need for sufficiently accurate aerodynamic analysis methods that go beyond the flat-plate analysis methods applied by Garrick and Bosch. The numerical methods should enable systematic studies of the effect of airfoil geometry, incidence angle variation, amplitude of oscillation, and airfoil interaction on the aerodynamic forces due to low-speed, viscous flows over airfoils or airfoil combinations executing pitch or plunge motions. In the past, Platzer et al.[9] first applied unsteady panel methods to this interference problem. Although the inviscid computations were promising, the viscous effects remained to be assessed.

It is the objective of the present work to demonstrate the feasibility of computing unsteady, viscous flowfields over flapping airfoils and flapping/stationary airfoil combinations in tandem (Fig. 1). To this end, a Navier–Stokes solver is primarily employed for the determination of the unsteady flowfields and aerodynamic forces in low subsonic flow. In the case of a single flapping airfoil, the computed results are compared against a potential flow solution. Unsteady aerodynamic interference effects and thrust generation on a flapping/stationary airfoil combination in tandem are computed by a multiblock version of the Navier–Stokes solver. In this case, the leading airfoil undergoes a flapping motion while the trailing airfoil is kept stationary. The leading airfoil serves as a vortex or gust generator that exposes the trailing airfoil to an oscillatory wake. The resulting gust response problem therefore is of very general interest with applications in the aircraft, missile, helicopter, and turbomachinery fields.

Numerical Methods

Unsteady, viscous flowfields around a single flapping airfoil and a flapping/stationary airfoil combination in tandem are primarily computed by a Navier–Stokes solver. For a single flapping airfoil, an unsteady potential flow solver (UPOT) is also utilized for comparison. In an earlier work, we have employed an interactive Navier–Stokes/potential flow solution method[10] for the flapping airfoils with success.[11]

In the case of flapping/stationary airfoil combinations in tandem, the multiblock version of the Navier–Stokes solver is employed. The computational domain is discretized with overlapping uniform grids around each airfoil, and the conservative flow variables are interpolated across overlapping grid boundaries as the grids move relative to each other along the unsteady motion.

Navier–Stokes Solution Method

The strong conservation-law form of the two-dimensional, thin-layer Navier–Stokes equations in a curvilinear coordinate system, (ξ, ζ), along the axial and normal direction, respectively, is given as follows:

$$\partial_t \hat{Q} + \partial_\xi \hat{F} + \partial_\zeta \hat{G} = Re^{-1} \partial_\zeta \hat{S} \qquad (1)$$
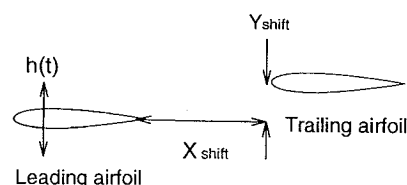
Fig. 1 Airfoil combination in tandem.

where $\hat{Q}$ is the vector of conservative variables $(\rho, \rho u, \rho w, e)/J$, $\hat{F}$ and $\hat{G}$ are the inviscid flux vectors, and $\hat{S}$ is the thin-layer approximation of the viscous fluxes in the ζ direction normal to the airfoil surface:

$$\hat{F} = \frac{1}{J} \begin{bmatrix} \rho U \\ \rho u U + \xi_x p \\ \rho w U + \xi_z p \\ (e+p)U - \xi_t p \end{bmatrix}, \quad \hat{G} = \frac{1}{J} \begin{bmatrix} \rho W \\ \rho u W + \zeta_x p \\ \rho w W + \zeta_z p \\ (e+p)W - \zeta_t p \end{bmatrix}$$

$$\hat{S} = \frac{1}{J} \begin{bmatrix} 0 \\ \mu m_1 u_\zeta + (\mu/3)m_2 \zeta_x \\ \mu m_1 w_\zeta + (\mu/3)m_2 \zeta_z \\ \mu m_1 m_3 + (\mu/3)m_2 + (\zeta_x u + \zeta_z w) \end{bmatrix}$$

where

$$m_1 = \zeta_x^2 + \zeta_z^2$$

$$m_2 = \zeta_x u_\zeta + \zeta_z w_\zeta$$

$$m_3 = \frac{u^2 + w^2}{2} + \kappa Pr^{-1}\left(\frac{\partial a^2}{\partial \zeta}\right)$$

and U and W are the contravariant velocity components, and Pr is the Prandtl number. The pressure p is related to density ρ and total energy e through the equation of state for an ideal gas, $p = (\gamma - 1)[e - \rho(u^2 + w^2)/2]$.

The flowfield is assumed to be fully turbulent, and the Baldwin–Lomax turbulence model is implemented.

Computational Grid

The computational domain is discretized by uniform C-grids. In the case of airfoils in tandem, individual C-grids are first generated around each airfoil. Depending on the specified distance between the airfoils, the grids are then overlapped at the downstream edge of the upstream grid and the upstream edge of the downstream grid as shown in Fig. 2.

This grid topology puts a heavy constraint on the computational grid around the downstream airfoil. On the downstream grid, as the grid extension in the normal direction drops from 8–10 chords lengths to less than 1 chord length upstream of the leading edge and the upstream outer boundary assumes a straight line, orthogonality of the upstream grid lines suffers considerably. The attempts made to generate a highly orthogonal, smoothly varying grid with parabolic and elliptic grid generators like GRAPE and GRIDGEN2D were not successful. In this study, an algebraic grid generator, which satisfies an orthogonality condition at the boundaries,[12] was adapted to generate the grid for the downstream airfoil.
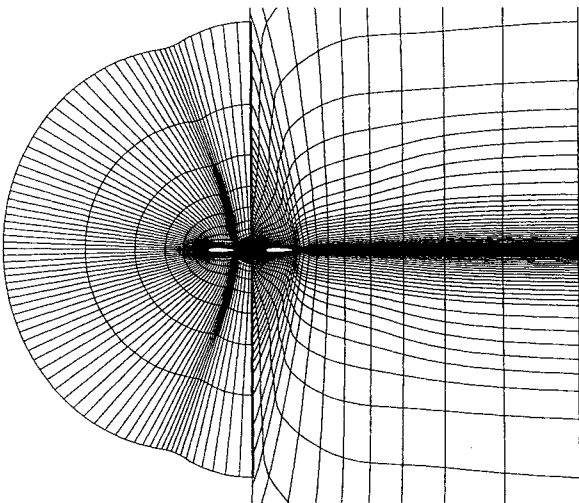

Fig. 2 Computational domain with overlapping C-grids. (Every other grid point is plotted.)

Boundary Conditions

The computational domain surrounds the airfoils and encompasses the viscous boundary-layer region and the wake regions. Boundary conditions are applied on the airfoil surfaces, along the overlapping grid boundaries and at the far-field boundaries.

On the airfoil surfaces the no-slip boundary condition is applied. For the leading airfoil, the surface fluid velocity is set equal to the prescribed airfoil flapping velocity so that the no-slip condition is satisfied. Since the formulation of the Navier–Stokes solver is based on an inertial frame of reference, the flapping motion is implemented by moving the airfoil and the computational grid around it in the transverse direction. The flapping motion is defined by

$$h = -A\cos(\omega t)$$

Here A denotes the mean amplitude normalized with the chord length; ω is the frequency of the oscillatory flapping motion, which is given in terms of the reduced frequency, $k = \omega c/2U_\infty$. The density and the pressure values on the airfoil surfaces are obtained from the interior by a simple extrapolation.

The boundary conditions at the overlapping intergrid boundary are applied by interpolating conservative flow variables across the boundary at every time step. Since the grids move relative to each other, the boundary points are first to be localized in terms of the neighboring grid points before the flow variables are interpolated. An overlapping boundary point on one of the grids is localized on the neighboring interpolation grid in terms of the closest three grid points. The flow variables, which are already computed on the interpolation grid, are then interpolated geometrically. The boundary points are localized with a sequential search algorithm, which is based on the gradients of the grid coordinates. Incidentally, the search algorithm also gives the interpolation weights as an integral part of the localization process. Since the overlapping boundary points are searched sequentially and the search algorithm is unified with the interpolation scheme, the application of the intergrid boundary conditions is quite robust and efficient.

At the far-field inflow and outflow boundaries the flow variables are evaluated using the zero-order Riemann invariant extrapolation. At the inflow boundary the density, the normal velocity and the pressure are specified, the tangential velocity is obtained from the Riemann invariant. At a subsonic outflow boundary only the pressure is specified while the density and the normal velocity is extrapolated from the interior. The tangential velocity is similarly obtained from the zero-order outgoing Riemann invariant.

Numerical Implementation

The numerical integration is performed using an upwind biased, factorized, iterative, implicit, numerical scheme[13,14] given by

$$\begin{aligned}
&\left[I + h_\xi\left(\nabla_\xi^b \tilde{A}_{i,k}^+ + \Delta_\xi^f \tilde{A}_{i,k}^-\right)\right]^p\left[I + h_\zeta\left(\nabla_\zeta^b \tilde{B}_{i,k}^+ + \Delta_\zeta^f \tilde{B}_{i,k}^-\right.\right. \\
&\left.\left. - Re^{-1}\delta_\zeta \tilde{M}_{i,k}\right)\right]^p\left(\tilde{Q}_{i,k}^{p+1} - \tilde{Q}_{i,k}^p\right) = -\left[\left(\tilde{Q}_{i,k}^p - Q_{i,k}^n\right) + h_\xi\right. \\
&\times \left(\hat{F}_{i+\frac{1}{2},k}^p - \hat{F}_{i-\frac{1}{2},k}^p\right) + h_\zeta\left(\hat{G}_{i,k+\frac{1}{2}}^p - \hat{G}_{i,k-\frac{1}{2}}^p\right) - Re^{-1}h_\zeta \\
&\left.\times \left(\hat{S}_{i,k+\frac{1}{2}}^p - \hat{S}_{i,k-\frac{1}{2}}^p\right)\right]
\end{aligned}$$

(2)

In Eq. (2), $h_\xi = \Delta\tau/\Delta\xi$, etc., and $\tilde{A}^\pm = (\partial \tilde{F}/\partial \tilde{Q})$, etc., are the flux Jacobian matrices, and Δ, ∇, and δ are the forward, the backward, and the central difference operators, respectively. The quantities $\tilde{F}_{i+1/2,k}$, $\tilde{G}_{i,k+1/2}$, and $\tilde{S}_{i,k+1/2}$ are numerical fluxes. The superscript n denotes the time step and p refers to Newton subiterations within each time step.

The inviscid fluxes $\hat{F}$ and $\hat{G}$ are evaluated using Osher's third-order-accurate upwinding scheme. For the linearization of the left-hand side of Eq. (2) the flux Jacobian matrices A and B are evaluated by the Steger–Warming flux-vector splitting. The viscous fluxes $\hat{S}$ are computed with second-order-accurate central differences.

Potential Flow Solution Method

In the potential flow solution (UPOT), the flowfield is assumed to be inviscid, irrotational, and incompressible. The unsteady flowfield

is represented by distributed source and vortex sheets on the airfoil surface and concentrated vortices in the wake. As the unsteady flow solution marches in time, a vortex is shed from the trailing edge of the airfoil and convected downstream with the local velocity. The velocity field is expressed in terms of a disturbance potential. Laplace's equation is then solved for the disturbance potential by superimposing the source/sink and vorticity singularity solutions to satisfy the boundary condition on the airfoil surface. This panel method has been developed by Teng[15] and has been applied successfully to various aerodynamic problems.

Results and Discussion

In the present study, we first investigated the thrust generated by a single flapping NACA 0012 airfoil. We then extended the investigation to the aerodynamic interaction between two NACA 0012 airfoils placed in tandem as the leading airfoil undergoes a flapping motion and its wake interacts with the trailing airfoil. In these cases, we parametrically studied the effects of the reduced frequency, the flapping amplitude, and X_{shift} and Y_{shift}, which define the offset position of the trailing airfoil from the mean position of the leading airfoil.

All of the flowfields were computed at $M_\infty = 0.3$ and $Re_c = 3.0 \times 10^6$. The airfoils were placed at 0-deg incidence at all times. Unsteady computations were initialized with steady-state flowfields computed at the minimum flapping amplitude, $h = -A$, where the flapping velocity is zero. The unsteady flow computations were then carried over more than three periods of the harmonic flapping motion. Data related to the flowfields were taken from the last cycle of computations.

The drag/thrust coefficient was evaluated by integrating the pressure distribution and thus represents only the pressure drag/thrust. The propulsive efficiency is defined as

$$\eta = (\bar{T} \cdot U_\infty / \bar{W})$$

where $\bar{T}$ is the average thrust and $\bar{W}$ is the average work required to maintain the flapping motion, which is computed by integrating the lift times the flapping velocity on the flapping airfoil. The time averaging is done over a period of the flapping motion.

Flapping Airfoil

In the following computations, a 181 × 81 point, C-type grid, which extends about 10 chord lengths (c) away from the airfoil, is used, and 120 of the grid points are around the airfoil. A grid study was made with a 281 × 81 grid, and the variation in the computed unsteady loads were found to be insignificant.

For a flapping motion of $A = 0.10c$ and $k = 1.5$, the flowfield computed by Navier–Stokes and the discrete wake vortices computed by UPOT are shown in Fig. 3 as the airfoil passes the mean position downward with the maximum flapping velocity. The size of the circles are proportional to the magnitude of the discrete vortex and the solid circles denote the clockwise vortices. As also observed in the wake velocity profiles, the flow at the trailing edge shoots upward like a jet and forms a strong counterclockwise vortex. The location of discrete vortices computed by UPOT agrees well with the viscous wake. The relative locations of counterclockwise and clockwise vortices with respect to the mean airfoil position are also in agreement with the observation made by Freymuth.[16] In his flow visualization studies, Freymuth identified the drag producing vortical flow pattern behind a stationary cylinder as compared with the thrust producing pattern behind a sinusoidally flapping airfoil. He observed that the cylinder produces a vortex street where the top vortices rotate clockwise and the bottom vortices counterclockwise; whereas in the wake of a thrust producing flapping airfoil counterclockwise rotating vortices are located at the top, above the mean flap position and vice versa.

The time history of unsteady aerodynamic loads and the flapping motion is shown in Fig. 4. Following the initial transition, all of the aerodynamic loads attain a periodic behavior with respect to the flapping motion. (Note that the amplitude of the flapping motion on the plot is not scaled.) The frequency of the drag/thrust coefficient is twice the flapping frequency since the maximum thrust is experienced as the airfoil passes the mean position upward and
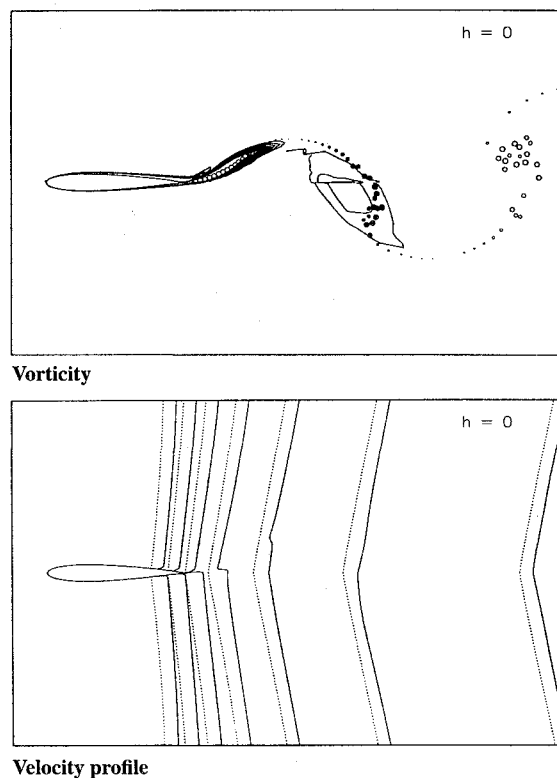

Fig. 3 Flowfield computed by Navier–Stokes and the discrete wake vortices computed by UPOT, $A = 0.10c$ and $k = 1.5$.
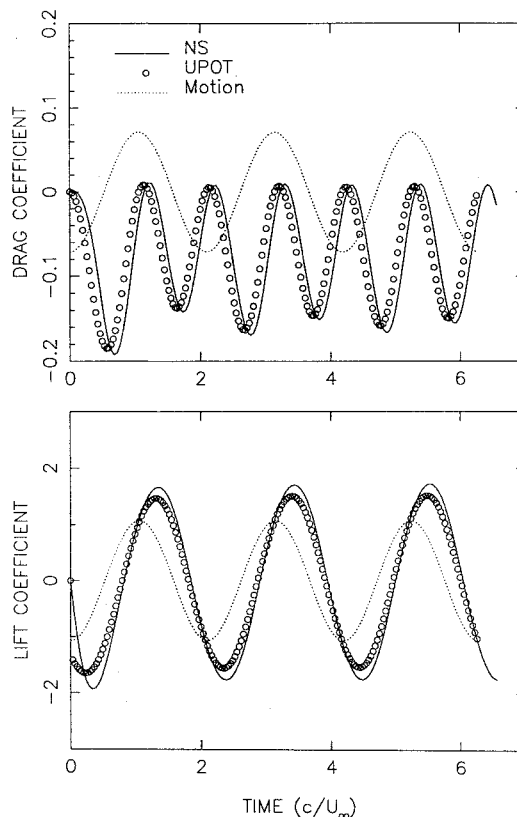

Fig. 4 Time history of the unsteady drag and lift coefficients, $A = 0.10c$ and $k = 1.5$.

downward in one period. The Navier–Stokes and UPOT predictions agree remarkably well.

The surface pressure distribution and the boundary-layer profiles on the upper surface as the airfoil passes the mean position downward are shown in Fig. 5. At this position of the airfoil, the thrust generation attains a maximum. As the pressure distributions predicted by Navier–Stokes also suggest, the boundary-layer profiles exhibit a
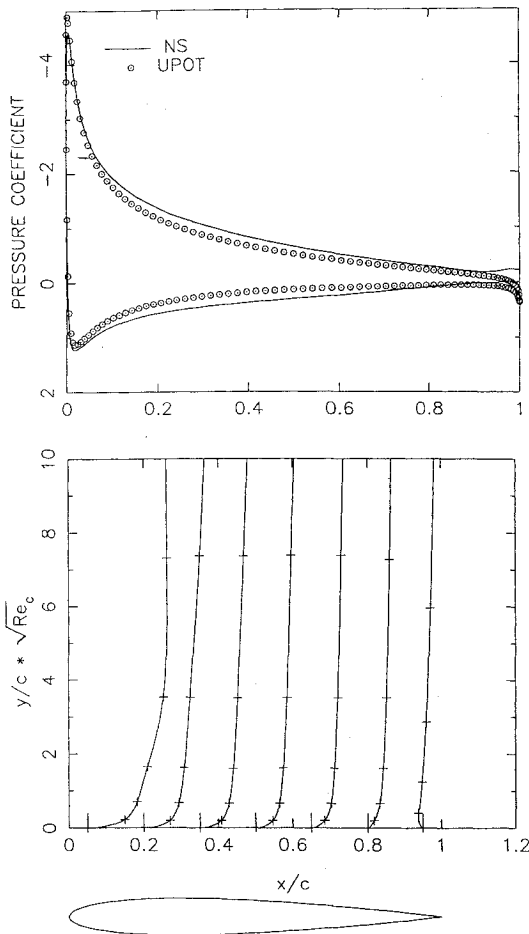
Fig. 5 Surface pressure distribution and boundary-layer profiles, $A = 0.10c$ and $k = 1.5$.

shallow flow reversal at the trailing edge that extends up to the 90% chord location. Note that the + sign on the boundary-layer profiles denotes every fifth grid point in the normal direction. Although the UPOT solution assumes an incompressible and a fully attached flow-field and consequently deviates from the Navier–Stokes and UPOT predictions slightly, the overall agreement is again very good.

The maximum suction peak attained at the leading edge appears to be sufficiently high, so that a thrust is generated. In addition, the thrust generating excess momentum manifests itself as a jetlike flow in the wake as observed in the wake velocity profiles in Fig. 3. Our computations suggest that while the jetlike velocity field around the trailing edge energizes the boundary layers and prevents trailing-edge flow separation, the high suction attained at the leading edge gives rise to thrust generation.

The average drag/thrust coefficients $\overline{C_D}$ and propulsive efficiency η computed at various reduced frequency and amplitudes are given in Fig. 6. The computed results are also compared against the lin-earized flat plate analysis of Bosch. As seen in the figures, linear theory gives the highest attainable average thrust and propulsive efficiency computed at all amplitudes and frequencies. The average thrust coefficient increases with reduced frequency and amplitude of the motion. The rate of increase with the amplitude assumes a quadratic trend as in the linear theory, although the computed rate drops at higher amplitudes compared with the linear theory.

On the other hand, the propulsive efficiency increases as the reduced frequency decreases and the flapping amplitude increases. The disagreement between the computed thrust coefficients and the linear theory at low reduced frequencies is caused by the smaller thrust coefficient predicted by the Navier–Stokes computations. Although the difference in magnitude of the thrust coefficient is about the same at high frequencies, combined with the relatively small lift coefficient it alters the propulsive efficiency significantly. It may be concluded that at low reduced frequency and amplitude flapping
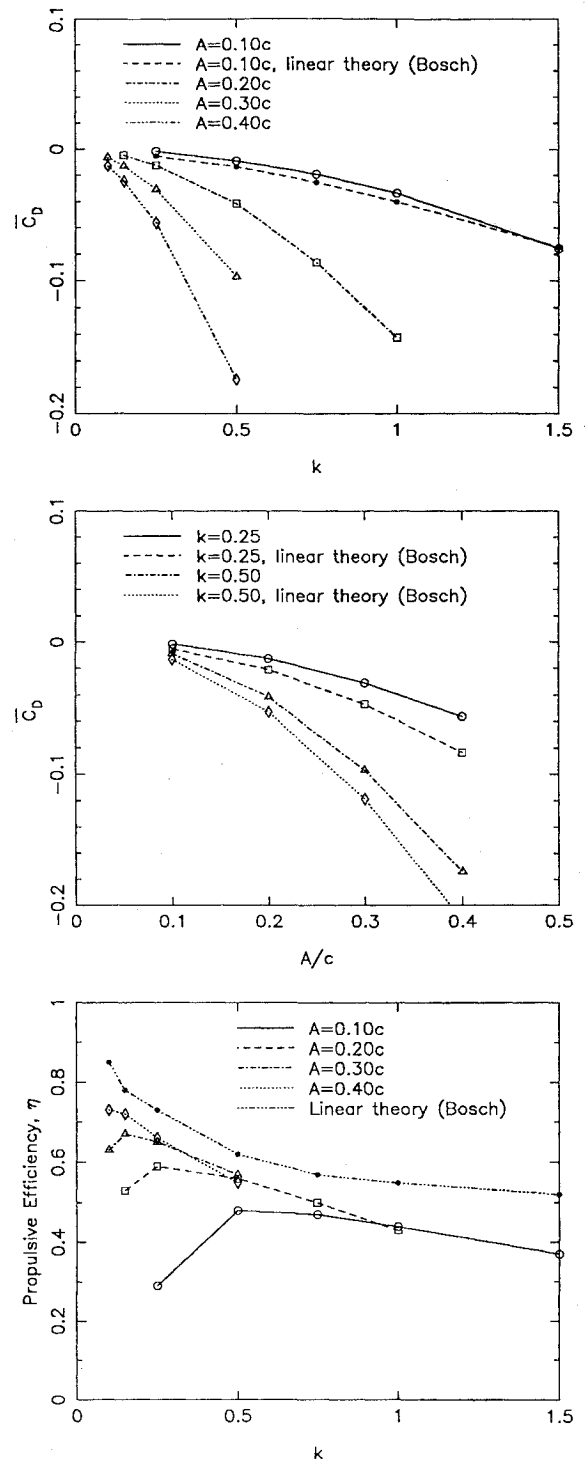

Fig. 6 Variation of propulsive efficiency and average drag/thrust coefficient with respect to flapping frequency and amplitude.

motions the viscous and nonlinear effects dominate the average thrust and reduce the propulsive efficiency significantly.

Flapping/Stationary Airfoil Combination

Next, we investigated the tandem airfoil configuration. In the computations, 161×61 and 181×71 point C-type grids were employed for the leading and trailing airfoils, respectively. A grid sensitivity study with clustering and the total number of grids points was performed on the trailing airfoil. It was found that the clustering of the grid points at the leading edge is critical and that coarser grids underpredict the leading-edge suction. The present grid clustering around the leading edge of the trailing airfoil is set to about $0.001c$. The grid spacing normal to the airfoil surfaces was set to about $0.00004c$.
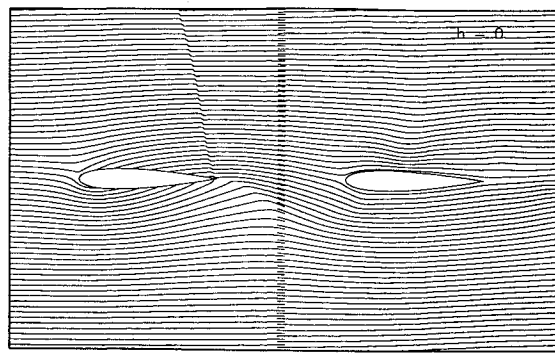
Mass-flux
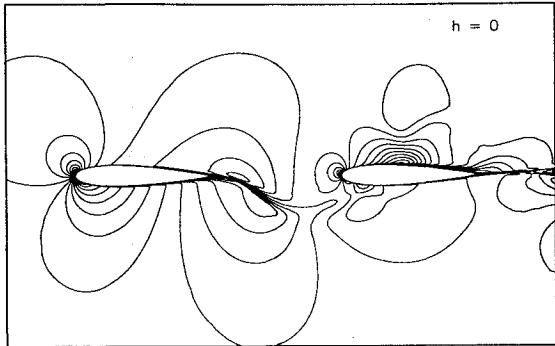
Mach number
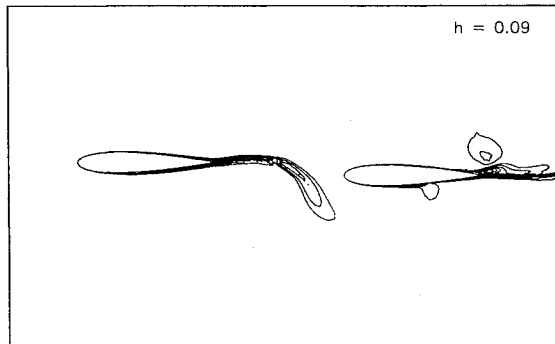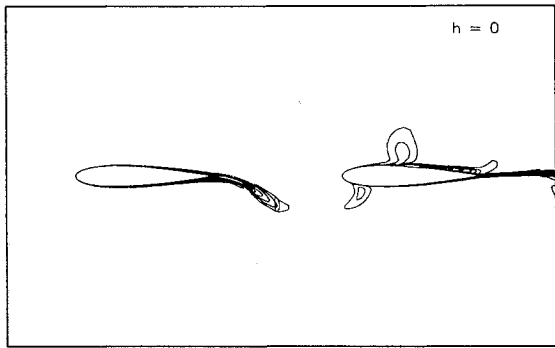
Vorticity

Fig. 7   Computed flowfield; $A = 0.10c$, $k = 1.5$, and $X_{\text{shift}} = 1.0c$.

First, we computed the flowfield as the trailing airfoil is placed one chord length from the leading airfoil, that is, $X_{\text{shift}} = 1.0c$ and $Y_{\text{shift}} = 0$, and k and A are set to 1.5 and 0.10c, respectively. Figure 7 shows the computed flowfield in terms of mass flux, Mach number, and vorticity contours as the leading airfoil passes through the mean position $h = 0$. The continuity of contour lines across the overlapping boundaries indicates that the overlapping boundary conditions are applied successfully. As seen in the vorticity field around the trailing airfoil, the vortices that are shed periodically from the leading airfoil interact strongly with the upper and lower boundary layers of the trailing airfoil. Also shown in the figure is the vorticity field close to the maximum amplitude $h = 0.099c$, which the airfoil reaches subsequently.
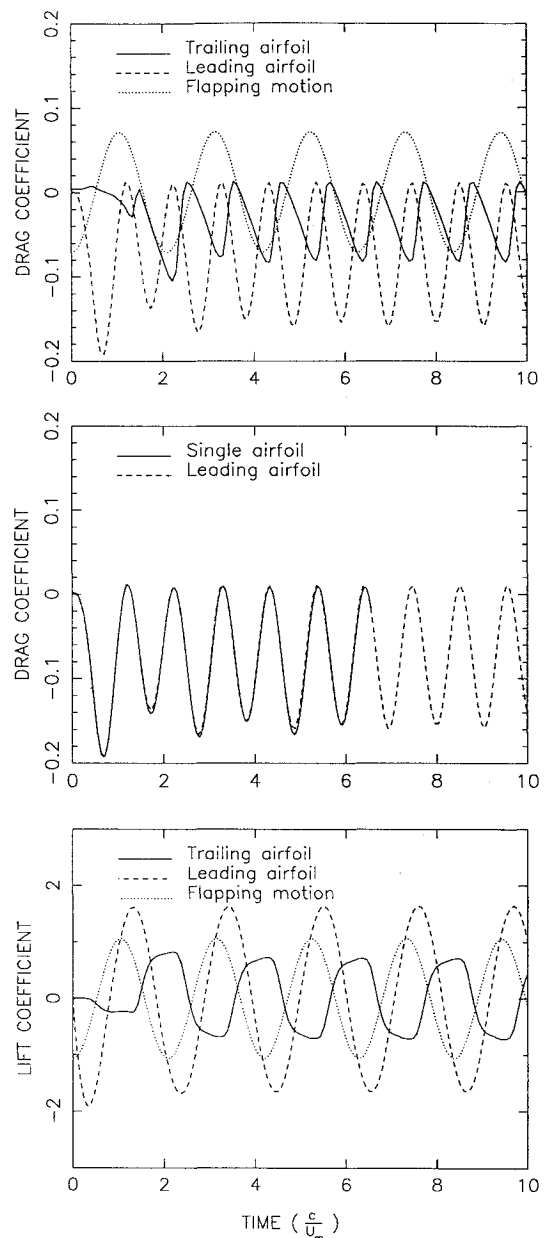
Fig. 8   Time history of the unsteady drag and lift coefficients; $A = 0.10c$, $k = 1.5$, and $X_{\text{shift}} = 1.0c$.

The time history of the aerodynamic forces on each airfoil is given in Fig. 8. Similarly, following the initial transient, all of the aerodynamic loads tend to attain a periodic behavior. As seen, both leading and trailing airfoils generate thrust. As observed in the second plot, the leading airfoil experiences the same thrust as the flapping single airfoil at the same frequency and amplitude, which we studied earlier. Thus, the thrust generated by the trailing airfoil is recovered from the excess momentum in the wake of the flapping airfoil and augments the total thrust of the airfoil combination significantly. The thrust on the trailing airfoil is generated when the vortical wake interacts with the airfoil. Figure 9 shows the vortical wake and the vortex induced flowfield around the leading edge of the trailing airfoil at the instant the trailing airfoil experiences the maximum thrust. At this instant, the strong counterclockwise vortex induces a favorable velocity field at the upper surface and causes a high leading-edge suction.

The surface pressure distributions and the boundary-layer profiles for the trailing airfoil at the positions producing maximum drag and thrust are shown in Fig. 10. The vortex induced suction peak and the energized boundary layers at the maximum thrust incidence are clearly seen in the figure.

For the present configuration and flow conditions, the propulsive efficiency of the leading airfoil alone and the airfoil combination

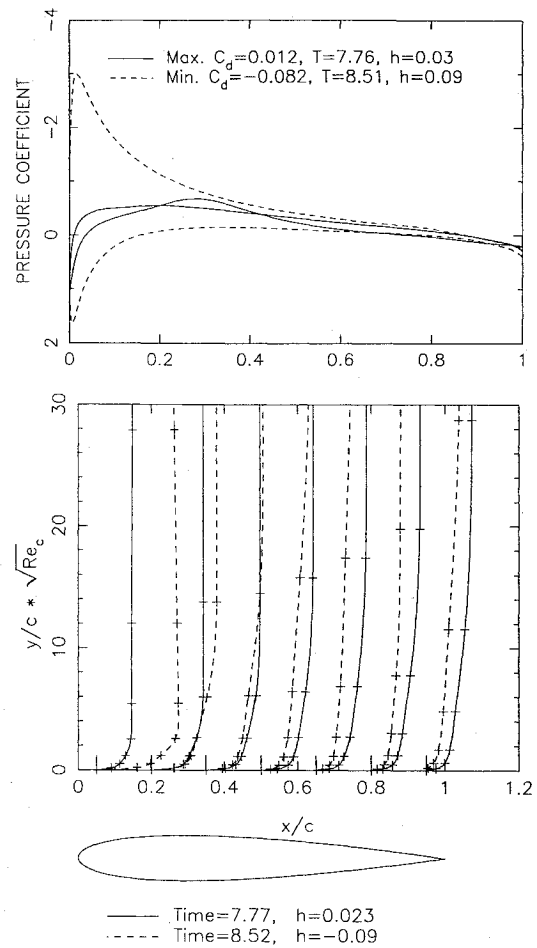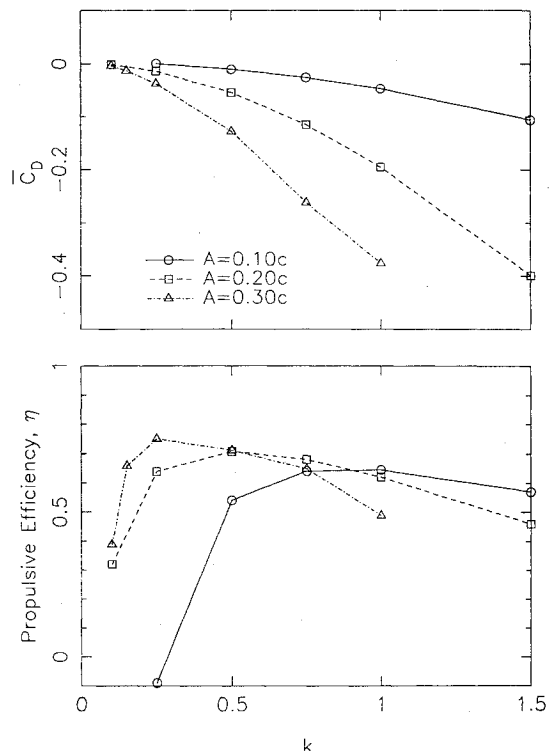**Table 1 Variation of the propulsive efficiency with X_{shift}**

| | $k = 0.75, A = 0.20c, Y_{shift} = 0.0$ | | | |
| | Leading airfoil | | Total | |
X_{shift}/c	η	$\overline{C}_D$	η	$\overline{C}_D$
0.65	0.50	−0.0900	0.67	−0.1197
1.00	0.50	−0.0838	0.68	−0.1149
1.50	0.50	−0.0808	0.69	−0.1116
2.00	0.50	−0.0817	0.70	−0.1132
3.00	0.50	−0.0837	0.68	−0.1139

Vorticity

Disturbance velocity
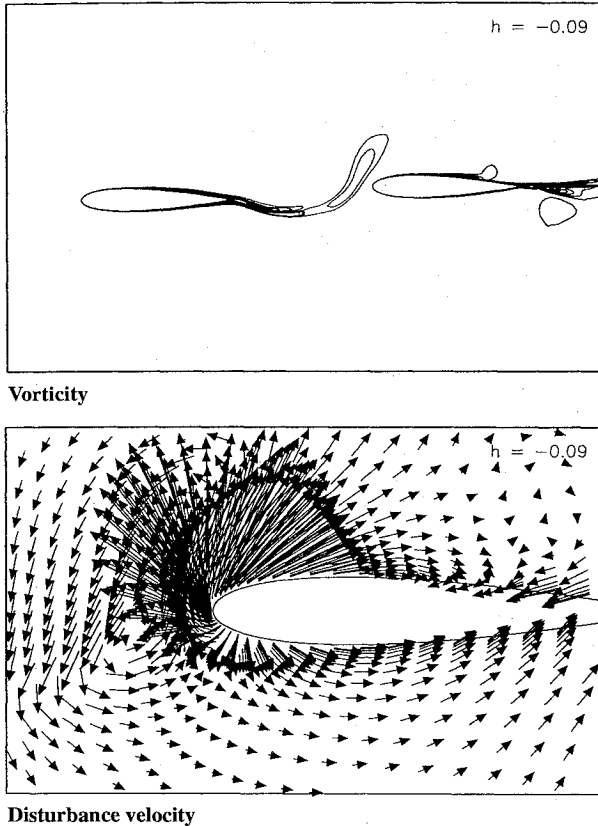
Fig. 9 Vorticity contours and disturbance velocity vectors around the leading edge of the trailing airfoil at time = 8.51 when the thrust is maximum; $A = 0.10c, k = 1.5$, and $X_{shift} = 1.0c$.

Fig. 10 Surface pressure distributions and boundary-layer profiles on the trailing airfoil; $A = 0.10c, k = 1.5$, and $X_{shift} = 1.0c$.

are computed to be 37 and 56%, respectively. The presence of the trailing airfoil thus enhances the propulsive efficiency quite significantly. These figures are, in general, in agreement with experiments by Schmidt.[5] He demonstrated that a stationary airfoil positioned in the wake of a flapping airfoil increases the propulsive efficiency up to 90% from less than 50% for the single flapping airfoil. Huyer and Luttges,[17] who examined the interaction at low Reynolds numbers between an oscillating upstream airfoil in pitch and a stationary trailing airfoil positioned at an angle of attack exceeding the static stall angle, also observed thrusting effects under certain test conditions.

Next, we investigated the variation of the propulsive efficiency on the other flow parameters, such as the flapping reduced frequency of the leading airfoil, k; the amplitude of the flapping motion, A; and the location of the trailing airfoil with respect to the leading airfoil as expressed by the terms X_{shift} and Y_{shift}. Figures 11–13 and Table 1 summarize the computed results. The average total drag coefficient is based on the chord length of the leading airfoil.

The variation of the average drag/thrust coefficient and the total propulsive efficiency with respect to the reduced frequency and amplitude of the flapping motion are given in Fig. 11, and they are compared against the single flapping airfoil in Fig. 12. As seen, at low reduced frequencies and amplitudes, such as $k = 0.25$ and $A = 0.10c$, the magnitude of the average thrust generated by the leading airfoil is insignificant, and there is no augmentation from the

Fig. 11 Variation of the total propulsive efficiency and the average thrust coefficient with the reduced frequency and amplitude of the flapping motion, $X_{shift} = 1.0c$ and $Y_{shift} = 0$.
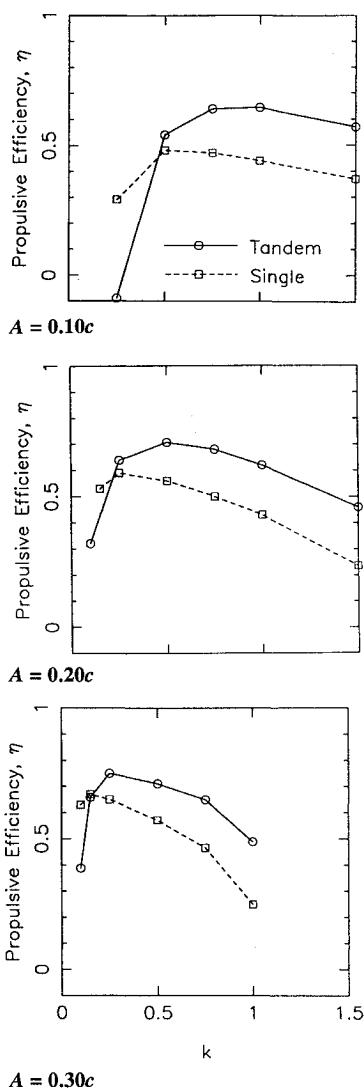
Fig. 12 Comparison of propulsive efficiency of the airfoil combination in tandem and the single airfoil, $X_{shift} = 1.0c$ and $Y_{shift} = 0$.
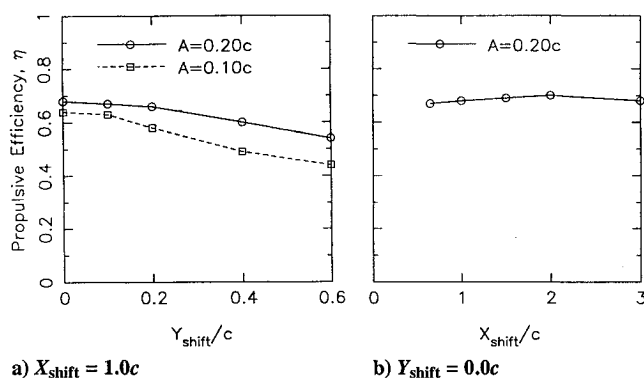

a) $X_{shift} = 1.0c$

b) $Y_{shift} = 0.0c$

Fig. 13 Variation of the total propulsive efficiency with Y_{shift} and X_{shift}, $k = 0.75$.

trailing airfoil. As a result the propulsive efficiency becomes negative; that is, the airfoil combination experiences drag. Similar to a single flapping airfoil the propulsive efficiency of an airfoil combination in tandem increases as the flapping amplitude increases and the reduced frequency decreases. However, the maximum efficiency at a constant flapping amplitude is shifted to a higher reduced frequency. For instance, at $A = 0.20c$ the propulsive efficiency of a single flapping airfoil is maximum at around $k = 0.25$, whereas the maximum efficiency for the airfoil combination is achieved at around $k = 0.50$ as shown in Fig. 12. Figure 12 also shows that at

low reduced frequencies the total propulsive efficiency is less than that of a single airfoil as the trailing airfoil experiences drag. Thus, the augmentation of thrust due to the trailing airfoil is not significant at low reduced frequencies.

Figure 13 and Table 1 show the effect of Y_{shift} and X_{shift}. In the case of various Y_{shift} offset locations of the trailing airfoil, the computational grids were obtained by merely shifting the downstream grid in the transverse direction. On the other hand, a new downstream grid had to be generated for each X_{shift} location.

As observed in Fig. 13, the thrust augmentation due to the trailing airfoil is maximum when the two airfoils are closely aligned but falls off significantly as the trailing airfoil is offset by more than the flapping amplitude A in the transverse direction. This is attributed to the trajectory of the shed vortices from the flapping airfoil. It appears that as long as the airfoils are not offset more than the amplitude of the flapping motion, there is a head-on collision of the wake vortices with the trailing airfoil. Therefore, the interaction between the trailing airfoil and the shed vortices is stronger when airfoils are closely aligned. The stronger is the interaction, the higher is the thrust augmentation. On the other hand, although the variation is relatively small, there is an optimum X_{shift} distance at which the total propulsive efficiency is maximized (Fig. 13b). It is also noted in Table 1 that for $X_{shift} = 0.65c$ the average thrust is the highest for both the leading and trailing airfoils. Yet this combination produces the lowest total propulsive efficiency. It appears that more work is required to flap the leading airfoil as the trailing airfoil is placed closer, which may be attributed to the blockage effect of the trailing airfoil in the near wake.

Concluding Remarks

Numerical solutions were obtained for low-speed flow over a flapping airfoil using a Navier–Stokes and a potential flow analysis. Both solutions were found to be in good agreement with each other, and they show that a flapping airfoil generates thrust and a distinct propulsive vortical flow pattern that is quite different from the typical drag producing vortical pattern generated by a stationary cylinder. As expected, the computed average thrust coefficients agree well with the linearized flat plate analysis at low-amplitude flapping motions.

Thrust enhancement in flapping/stationary airfoil combinations in tandem was next investigated using a zonal Navier–Stokes solver only. The computations identified the interaction between the shed vortices and the trailing airfoil and confirmed the previous experimental and inviscid flow predictions that the presence of a stationary airfoil in the wake of a flapping airfoil enhances the total thrust and propulsive efficiency significantly. It was found that the augmentation of thrust due to the trailing airfoil is most significant at relatively high reduced frequencies. In addition, the augmentation is maximum when the airfoils are aligned and drops off significantly as the trailing airfoil is offset by more than the flapping amplitude in the transverse direction. The thrust augmentation due to a trailing airfoil did not strongly depend on the distance between the airfoils in the range studied.

Acknowledgments

References

[1]Knoller, R., "Die Gesetze des Luftwiderstandes," *Flug-und Motortechnik (Wien)*, Vol. 3, No. 21, 1909, pp. 1–7.

[2]Betz, A., "Ein Beitrag zur Erklaerung des Segelfluges," *Zeitschrift fur Flugtechnik und Motorluftschiffahrt*, Vol. 3, Jan. 1912, pp. 269–272.

[3]Von Kármán, T., and Burgers, J. M., *Aerodynamic Theory*, Vol. 2, Springer, Berlin, 1935, pp. 280–310.

[4]Garrick, I. E., "Propulsion of a Flapping and Oscillating Airfoil," NACA Rept. 567, 1936.

[5]Schmidt, W., "Der Wellpropeller, ein neuer Antrieb fuer Wasser-, Land-, und Luftfahrzeuge," *Zeitschrift fur Flugwiss*, Vol. 13, Dec. 1965, pp. 472–479.

[6]Bosch, H., "Interfering Airfoils in Two-Dimensional Unsteady, Incompressible Flow," AGARD-CP-227, Feb. 1978.

[7]Wood, E. R., Powers, R. W., Cline, J. H., and Hammond, C. E., "On Developing and Flight Testing a Higher Harmonic Control System," *Journal of the American Helicopter Society*, Vol. 30, No. 2, 1985, pp. 3–20.

[8]Wood, E. R., Platzer, M. F., Abourahma, A., and Couch, M. A., "On the Unsteady Aerodynamics of Higher Harmonic Control," Nineteenth European Rotorcraft Forum, Cernobbio, Italy, Paper C17, Sept. 1993.

[9]Platzer, M. F., Neace, K. S., and Pang, C. K., "Aerodynamic Analysis of Flapping Wing Propulsion," AIAA Paper 93-0484, Jan. 1993.

[10]Tuncer, I. H., Ekaterinaris, J. A., and Platzer, M. F., "Viscous-Inviscid Interaction Method for Unsteady Low-Speed Airfoil Flows," *AIAA Journal*, Vol. 33, No. 1, 1994, pp. 151–154.

[11]Tuncer, I. H., Ekaterinaris, J. A., and Platzer, M. F., *Computational Analysis of Flapping Airfoil Aerodynamics*, Advances in Computational Methods in Fluid Dynamics, American Society of Mechanical Engineers, New York, FED-Vol. 196, 1994, pp. 9–18.

[12]Fletcher, C. A. J., *Computational Techniques for Fluid Dynamics*, Vol. 2, 2nd ed., Springer–Verlag, Berlin, 1991, p. 115.

[13]Rai, M. M., and Chakravarthy, S. R., "An Implicit Form of the Osher Upwind Scheme," *AIAA Journal*, Vol. 24, No. 5, 1986, pp. 735–743.

[14]Ekaterinaris, J. A., Cricelli, A., and Platzer, M. F., "A Zonal Method for Unsteady, Viscous, Compressible Airfoil Flows," *Journal of Fluids and Structures*, Vol. 8, Jan. 1994, pp. 107–123.

[15]Teng, N. H., "The Development of a Computer Code (U2DIFF) for the Numerical Solution of Unsteady, Inviscid and Incompressible Flow over an Airfoil," Thesis, Dept. of Aeronautics and Astronautics, U.S. Naval Postgraduate School, Monterey, CA, June 1987.

[16]Freymuth, P., "Propulsive Vortical Signature of Plunging and Pitching Airfoils," *AIAA Journal*, Vol. 26, No. 7, 1988, pp. 881–883.

[17]Huyer, S. A., and Luttges, M. W., "Unsteady Flow Interactions Between the Wake of an Oscillating Airfoil and a Stationary Trailing Airfoil," AIAA Paper 88-2581, July 1988.